JMEPEG (2010) 19:488–494
DOI: 10.1007/s11665-010-9612-6

1059-9495/$19.00

Material Models for Simulation of Superplastic Mg Alloy Sheet Forming

Eric M. Taleff, Louis G. Hector Jr., Ravi Verma, Paul E. Krajewski, and Jung-Kuei Chang

(*Submitted December 9, 2009; in revised form January 4, 2010*)

Accurate prediction of strain fields and cycle times for fine-grained Mg alloy sheet forming at high temperatures (400-500 °C) is severely limited by a lack of accurate material constitutive models. This paper details an important first step toward addressing this issue by evaluating material constitutive models, developed from tensile data, for high-temperature plasticity of a fine-grained Mg AZ31 sheet material. The finite element method was used to simulate gas pressure bulge forming experiments at 450 °C using four constant gas pressures. The applicability of the material constitutive models to a balanced-biaxial stress state was evaluated through comparison of simulation results with bulge forming data. Simulations based upon a phenomenological material constitutive model developed using data from both tensile elongation and strain-rate-change experiments were found to be in favorable accord with experiments. These results provide new insights specific to the construction and use of material constitutive models for hot deformation of wrought, fine-grained Mg alloys.

Keywords biaxial stress, fine grain, finite element, Mg AZ31 alloy, modeling, PAM-STAMP 2G™, quick plastic forming

1. Introduction

With a density that is two-thirds that of aluminum (Al), one-quarter that of steel, and a high strength-to-weight ratio, magnesium (Mg) alloys such as AZ31 (3% Al, 1% Zn) hold great promise for reducing vehicle weight and improving fuel economy without compromising passenger safety and comfort. By taking advantage of commercial fine-grained Mg alloys, substantial progress in the high-temperature forming of Mg vehicle closure components has been made. A specific example using the Quick-Plastic Forming (QPF) process (Ref 1) with a commercial-grade Mg AZ31 alloy sheet is detailed in Ref 2. These promising results have not only brought the implementation of Mg sheet alloys in vehicles much closer to reality, they represent what is a likely "industry first" in automotive manufacturing.

A major advantage of the QPF process is that it can produce complex components from Mg alloy sheet, which cannot be readily formed at room temperature. In addition, the QPF forming conditions provide part cycle times that are much shorter than those associated superplastic forming (SPF). The part consolidation possible with QPF can eliminate multiple forming and joining steps, further reducing part weight. While substantial progress has been made in the development of QPF for Mg alloy closures through experimental means, future enhancements to such critical process variables as gas pressure profiles and sheet/die friction can be facilitated with the remarkable advances in computer simulation technologies, such as the finite element method (FEM). In addition, better estimates of part production costs are possible through accurate simulations. Despite the considerably advanced simulation technologies available in commercial finite element (FE) computer codes, such as PAM-STAMP 2G 2007™ (Ref 3) and ABAQUS6.5.6™ (Ref 4), one of the greatest hurdles for Mg alloy forming simulations is the development of accurate material constitutive models. These must correctly capture microstructural deformation mechanisms active in Mg alloys at the elevated temperatures typical for QPF and provide the correct material responses under the multiaxial stress states and through the complex strain paths typical of QPF. This is especially important for the current Mg sheet alloys, as they are notoriously difficult to form at room temperature due to a strong basal texture, anisotropic properties and twinning deformation. Such features are peculiar to the hexagonal-close-packed (HCP) crystal structure of Mg (Ref 5). Deformation at elevated temperatures in the vicinity of 450 °C greatly minimizes, or even eliminates, many of these issues and introduces a high strain-rate sensitivity leading to enhanced ductility.

In this paper, we develop high-temperature material constitutive models for the fine-grained Mg AZ31 sheet described in Ref 5. Tensile strain-rate-change tests and tensile elongation tests were used to construct these models (Ref 6), as is common practice in studies of high-temperature material model development and deformation (Ref 7-14). We use these models to simulate gas-pressure bulge forming, a simple bench-scale test of sheet materials which produces a nearly balanced-biaxial

This article is based on a presentation at the AeroMat Conference, International Symposium on Superplasticity and Superplastic Forming (SPF) held in Austin, TX, June 23-26, 2008.

Eric M. Taleff and **Jung-Kuei Chang**, Mechanical Engineering, The University of Texas at Austin, 1 University Station C2200, Austin, TX 78712; and **Louis G. Hector Jr., Ravi Verma,** and **Paul E. Krajewski**, General Motors Corp., Research and Development, MC 480-106-212, 30500 Mound Rd., Warren, MI 48090-9055. Contact e-mail: louis.hector@gm.com.

stress, at 450 °C. The material constitutive models were implemented as user subroutines in the finite element (FE) codes PAM-STAMP 2G™ (Ref 3) (explicit solver) and ABAQUS 6.5.6™ (implicit solver) (Ref 4). The extent to which the material constitutive models accurately describe high-temperature deformation of the Mg sheet material is evaluated through critical comparison of simulation results with experimental data. We note that there are currently very few references detailing material models for high-temperature forming of AZ31 sheet. Of these, Ref 15, 16 are notable as they detail a set of tensile strain-rate-change tests of AZ31 sheet aimed at development of a phenomenological material model for superplastic forming conditions (i.e. slower deformation rates and higher forming temperatures than those associated with QPF). These authors also explored AZ31 bulge forming with the same material model using a tensile stability criterion to determine optimum formability with predicted gas-pressure profiles (Ref 17).

2. Experimental Procedures

Tensile strain-rate-change (SRC) tests, tensile tests and gas-pressure bulge-forming tests were conducted on a fine-grained, $d \approx 9$ μm, AZ31 sheet with a 2.0-mm initial thickness. Table 1 details the material composition. Tensile SRC tests and tensile tests were conducted using a forced air furnace, which maintained temperature to within approximately ±1 °C, attached to a computer-controlled, screw-driven testing machine. Tensile SRC coupons with a gage length of 25.4 mm and a gage width of 6.35 mm, retaining the as-received thickness of 2 mm, were machined from the sheet with the tensile axis parallel to the rolling direction of the sheet. These tensile coupons were subjected to tensile SRC tests at temperatures of 350, 400, 450, and 500 °C (Ref 6). These SRC tests consisted of an initial prestrain of 5 to 10% elongation, followed by a series of six steps at different strain rates, with fast rates preceding the slow rates. The six strain rates in each series ranged from 3×10^{-2} to 10^{-4} s^{-1}, and the initial strain-rate series was repeated twice for each test with load and elongation measured during each step. From these SRC data, true flow stress was calculated at each strain rate for true strains of 0.2, 0.4, and 0.6 by interpolation in strain. Tensile tests were conducted at a temperature of 400 °C and at engineering strain rates of 3×10^{-3} and 3×10^{-4} s^{-1} to elongations equivalent to a true strain $\varepsilon = 0.4$. Tensile coupons for these tests were machined with a gage width of 6 mm and a gage length of 25 mm, retaining the as-received thickness of 2 mm, with the tensile axis parallel to the rolling direction.

Gas-pressure bulge-forming experiments were conducted on square blanks approximately 175 × 175 mm on edge, which were cut from the same AZ31 sheet material used for the tension tests. In each experiment, a single blank was pre-heated in the forming die to 450 °C. Additional details on the cylindrical die geometry may be found in Ref 18. The temperature was allowed to equilibrate for approximately 5 min prior to testing. Gas pressure was then quickly ramped (manually) to a predetermined value and held constant for the duration of the experiment. This caused the sheet to bulge into a 100-mm cylindrical die opening, which has a 5-mm entry radius. Gas pressures of 450 kPa (65 psi), 480 kPa (70 psi), 830 kPa (120 psi) and 900 kPa (130 psi) were used in the tests. Each experiment was either terminated at a predetermined forming time or continued until the dome ruptured. Dome height and dome pole thickness were measured after each experiment. Rupture times at each of the four test pressures are detailed in Table 2.

3. Finite Element Simulations

Finite element simulations were conducted with two commercial software packages, PAM-STAMP 2G 2007™ (Ref 3) (explicit formulation) and ABAQUS 6.5.6™ (Ref 4) (implicit formulation). The material constitutive models developed for this study were implemented via a user subroutine in both codes and compiled in at run time. Details of the simulation methods, element types and meshes are the same as those previously used for AA5083 sheet (Ref 18). Differences from previous studies include use of new material models, a new initial sheet thickness of 2 mm and forming pressures and times specific to the AZ31 experimental data (see Table 2). Predicted dome pole height and dome pole thickness were taken from the simulations as functions of time for comparison with data from the bulge experiments.

4. AZ31 Magnesium Material Model

The flow stresses measured in the tensile SRC tests at a given strain rate, associated with a different strain in each step series, were used to linearly interpolate the flow stress at true strains of 0.2, 0.4 and 0.6. The SRC test data are reported in Fig. 1 as logarithm of true strain rate versus logarithm of true stress. Strain hardening, an increase in flow stress with strain, is evident at the slowest strain rates and highest temperatures. Note, for example, the increasing flow stress at labeled strains of 0.4 (blue) and 0.6 (red) in Fig. 1. Strain hardening is frequently observed in superplastic materials as a result of dynamic grain growth when deformation is by grain-boundary-sliding (GBS) creep.

Data from tensile tests at 400 °C are shown in Fig. 2 as true stress versus true strain. Measurements of tensile coupon cross

Table 2 Gas pressures used and failure times recorded in the AZ31 bulge forming experiments

Pressure, kPa	450	480	830	900
Failure time, s	1534	1323	235	142

Table 1 Composition of the AZ31 material in wt.%

Element	Al	Zn	Mn	Fe	Cu	Ni	Si	Ca	Be	Sr	Ce	Mg
Wt.%	3.1	1.0	0.42	0.006	0.003	<0.003	<0.1	<0.01	<0.005	<0.005	<0.01	Bal.

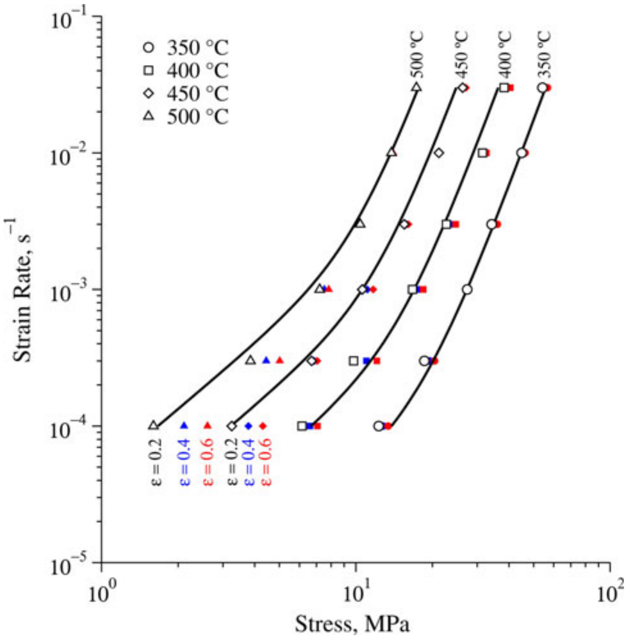

Fig. 1 Data from SRC tests of the AZ31 material at four different temperatures are shown. The strain markers indicate the strain to which flow stress was interpolated. Data are shown interpolated to ε = 0.2 (*black*), ε = 0.4 (*blue*) and ε = 0.6 (*red*). Curves are from the constitutive material model (Eq 1), which was fit to data from the first strain-rate series (ε = 0.2) at each test temperature

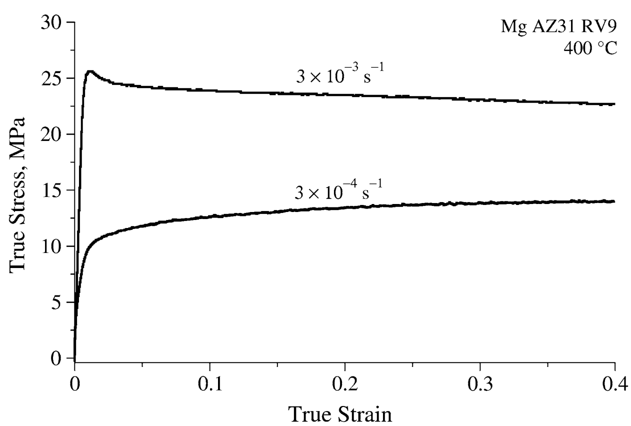

Fig. 2 Data from tension tests of the AZ31 material at 400 °C and two different engineering strain rates are shown as true stress against true strain

sections following testing to a true strain of 0.4 revealed an anisotropy factor, $R = \varepsilon_{width}/\varepsilon_{thickness}$, of unity for each test. This suggests isotropic deformation with respect to the 0° and 90° orientations and the thickness direction (0° is along the tensile axis). It is also of note that a region of rapid strain softening follows the initial stress transient at the beginning of the elongation test at 3×10^{-3} s^{-1}, shown in Fig. 2, but it is not apparent at 3×10^{-4} s^{-1}. This could be a result of GBS creep dominating flow at the slow rate and dislocation creep dominating flow at the fast rate.

Data from tensile SRC tests (Fig. 1) were used to construct a constitutive material model for the AZ31 sheet material at temperatures ranging from 350 to 500 °C. Fast strain rates and low temperatures, e.g. 0.3 s^{-1} and 350 °C, correspond to a high Zener-Hollomon parameter, $Z = \dot{\varepsilon} \times \exp(Q_c/RT)$, where $\dot{\varepsilon}$ is true-strain rate, Q_c is the activation energy for creep, and T is absolute temperature. The stress exponent is approximately $n = 5.0$ for high Z, and this value of n is often associated with dislocation slip creep, for which the deformation rate is controlled by dislocation climb (Ref 19). Alternatively, the stress exponent is between 1.0 and 2.0 at low Z, e.g. 10^{-4} s^{-1} and 500 °C, and such n values are often associated with GBS creep (Ref 20). Different Q_c values were measured in these two regimes. At high Z, $Q_c = 138$ kJ/mole, and at low Z, $Q_c = 91$ kJ/mole. The high- and low-Z regions are interpreted as representing two distinct, competitive creep deformation mechanisms. Consistent with this interpretation, a two-mechanism phenomenological equation for creep deformation was used to formulate a constitutive model of AZ31 material behavior at 450 °C. This is the same basic form as was previously used for fine-grained AA5083 sheet material (Ref 18, 21). The model was fit to the data in Fig. 1 at a true strain of ε = 0.2 by constructing separate fits at high Z and at low Z, with each fit applying to one of the two creep deformation mechanisms. Data at a strain of 0.2 were used for initial model formulation with full realization that strain hardening, or other effects, might require later modifications. The resulting relationship for strain rate, $\dot{\varepsilon}$ (s^{-1}), is

$$\dot{\varepsilon} = 7.494 \times 10^{8}\left(\frac{\sigma}{E}\right)^{1.57}\exp\left(-\frac{Q_1}{RT}\right) + 2.517 \times 10^{24}\left(\frac{\sigma}{E}\right)^{5.10}\exp\left(-\frac{Q_2}{RT}\right) \qquad \text{(Eq 1)}$$

where $Q_1 = 91$ kJ/mole, $Q_2 = 138$ kJ/mole, σ is true flow stress in MPa and E is the dynamic unrelaxed temperature-dependent Young's modulus, taken as equal to that of pure Mg. The temperature-dependent elastic modulus of pure Mg, as taken from a fit to the data of Köster (Ref 22), is given in MPa by

$$E(T) = 48,700 - 8.59T - 0.0195T^2 \qquad \text{(Eq 2)}$$

where T is in Kelvin. The fit of Eq 1 to the strain-rate-change test data is shown as the solid curves in Fig. 1; these are in close agreement with the associated SRC data for ε = 0.2. Equation 1 was used to generate the following relationship at 450 °C, which is the first material constitutive model used in finite element simulations:

$$\dot{\varepsilon} = 1.585 \times 10^{-5}\sigma^{1.57} + 2.139 \times 10^{-9}\sigma^{5.10} \qquad \text{(Eq 3)}$$

A second constitutive model was constructed based on the plot shown in Fig. 3, which includes SRC data at 400 °C and flow stress data taken from the two tensile tests shown in Fig. 2. The tensile tests clearly produce higher flow stresses at slow strain rates, where GBS creep is expected, than do the SRC tests at equivalent strains. At fast strain rates, where dislocation creep is expected, the flow stresses produced by the two test types are similar. To make the simplest possible evaluation of these effects in the simulation, and to retain the temperature dependence of the initial model, the second model was constructed by simply increasing predicted flow stress from Eq 1 by 30%. This modified model, referred to herein as the "1.3 σ model," is shown as a dashed curve in Fig. 3 and was implemented into PAM-STAMP 2G 2007™.

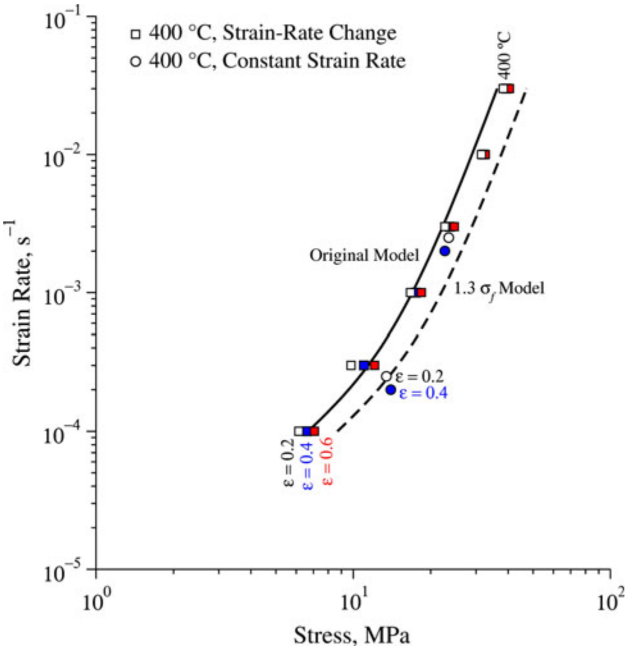

Fig. 3 SRC and tension test data at 400 °C are shown. The constitutive model constructed initially from SRC data (Eq 1) is shown as a *solid curve*. The 1.3 α model (Eq 4) is shown as a *dashed curve*

This was accomplished by multiplying flow stress by 1.3 in the array of user material model data, producing the following equation form at 450 °C,

$$\dot{\varepsilon} = 1.05 \times 10^{-5}\sigma^{1.57} + 5.61 \times 10^{-10}\sigma^{5.10} \quad \text{(Eq 4)}$$

We note that this modified model better fits tensile test results at low Z values in Fig. 3, but fits less well at high Z. Simulations were then conducted at the lowest (450 kPa) and highest (900 kPa) gas pressures for comparison with experimental data and simulation results based upon Eq 3.

5. Finite Element Simulation Results

Figure 4 shows FE simulation results at 450 °C for dome pole height as a function of forming time at constant gas pressures of 450 kPa (65 psi), 480 kPa (70 psi), 830 kPa (120 psi) and 900 kPa (130 psi), respectively. The solid (PAM-STAMP 2G 2007™) and dashed (ABAQUS 6.5.6™) curves in Fig. 4 correspond to FE predictions based upon the material model of Eq 3. Small differences between the curves from the two codes also appear and are attributable to differences in finite element formulations and the fact that an initial elastic phase of deformation is applied to the sheet in the ABAQUS™ simulations to eliminate the normal direction singularity

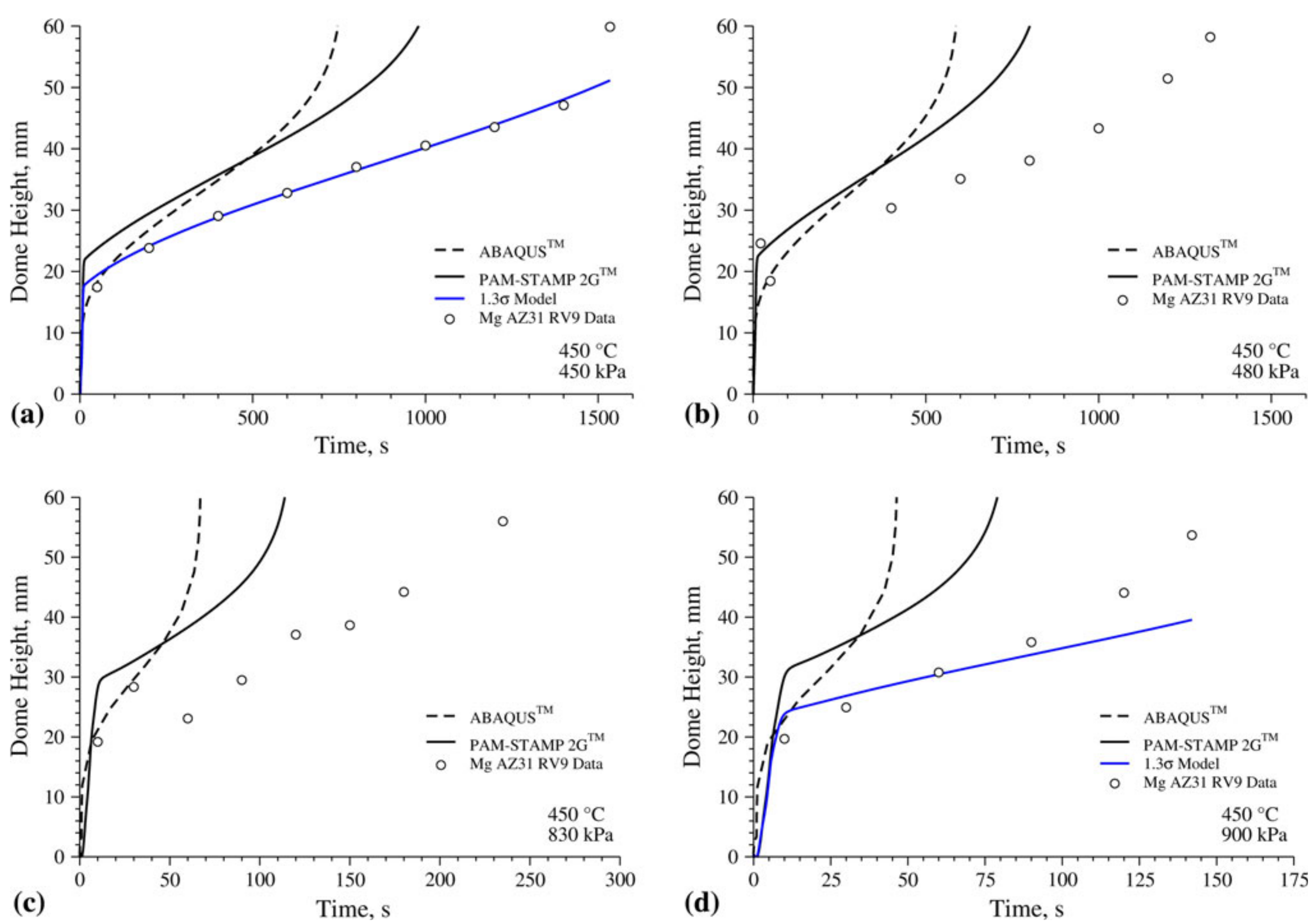

Fig. 4 Predictions for AZ31 dome pole height as a function of forming time are shown along with experimental bulge data at 450 °C, (a) 450 kPa (65 psi), (b) 480 kPa (70 psi), (c) 830 kPa (120 psi), and (d) 900 kPa (130 psi)

condition due to the initially flat sheet geometry. A similar phase is unnecessary in PAM-STAMP 2G 2007™ since assembly of a stiffness matrix is avoided. Also included in each plot are experimental data points from AZ31 bulge forming experiments. While the simulation results from both FE codes are similar, we note that in each case they predict a much more rapid dome height increase with forming time than is observed in the experiments. These differences are largest at the highest gas pressures (cf. Fig. 4a, d).

Figure 5 shows FE simulation results for dome pole thickness as a function of time at the four pressures using the material model of Eq 3. The simulations predict more rapid thinning at the dome pole than observed in the experiments, with ABAQUS™ predicting even more rapid thinning than PAM-STAMP 2G™. Again, deviations between the predicted and experimentally observed pole thickness are largest for the greatest forming pressures.

The simple shift to higher flow stresses provided by the 1.3 σ model brings the simulations using PAM-STAMP 2G™ (blue curves in Fig. 4a, d and 5a, d) into close agreement with the experimental data at the lowest (450 kPa) and highest (900 kPa) forming pressures. These results warrant additional comment. The average thickness true-strain rates experimentally produced at these two pressures, calculated from pole thinning and time at rupture, are 0.001 s^{-1} at 450 kPa and 0.01 s^{-1} at 900 kPa. At the lowest forming pressure, strain hardening during GBS deformation may be expected from the experimental data of Fig. 1-3. However, those same data give no indication of any hardening at the fast strain rate produced by the highest pressure, where slip creep is expected. Thus, the success of the 1.3 σ model (Eq 4) over the original material model of Eq 3 must be considered largely phenomenological and somewhat unexpected.

6. Discussion

Material models for fine-grained aluminum alloy AA5083 sheet input to the PAM-STAMP 2G™ and ABAQUS™ FE packages have been shown to accurately predict bulge dome heights and pole thinning at 450 °C only if the threshold stress for GBS is neglected (Ref 18). These simulations suggested that hydrostatic stress has an appreciable effect on grain-boundary sliding (GBS) in AA5083. An increase in the hydrostatic stress appears to increase the plastic strain rate by reducing the threshold stress for GBS. While more appropriate for tensile deformation, a threshold stress term for AA5083 predicts slower flow in biaxial tension than what is observed in experiments. Hence, a zero threshold stress gave the best agreement with experiment for AA5083 (Ref 18). Despite the fact that Eq 3 neglects threshold stress, the FE predictions of

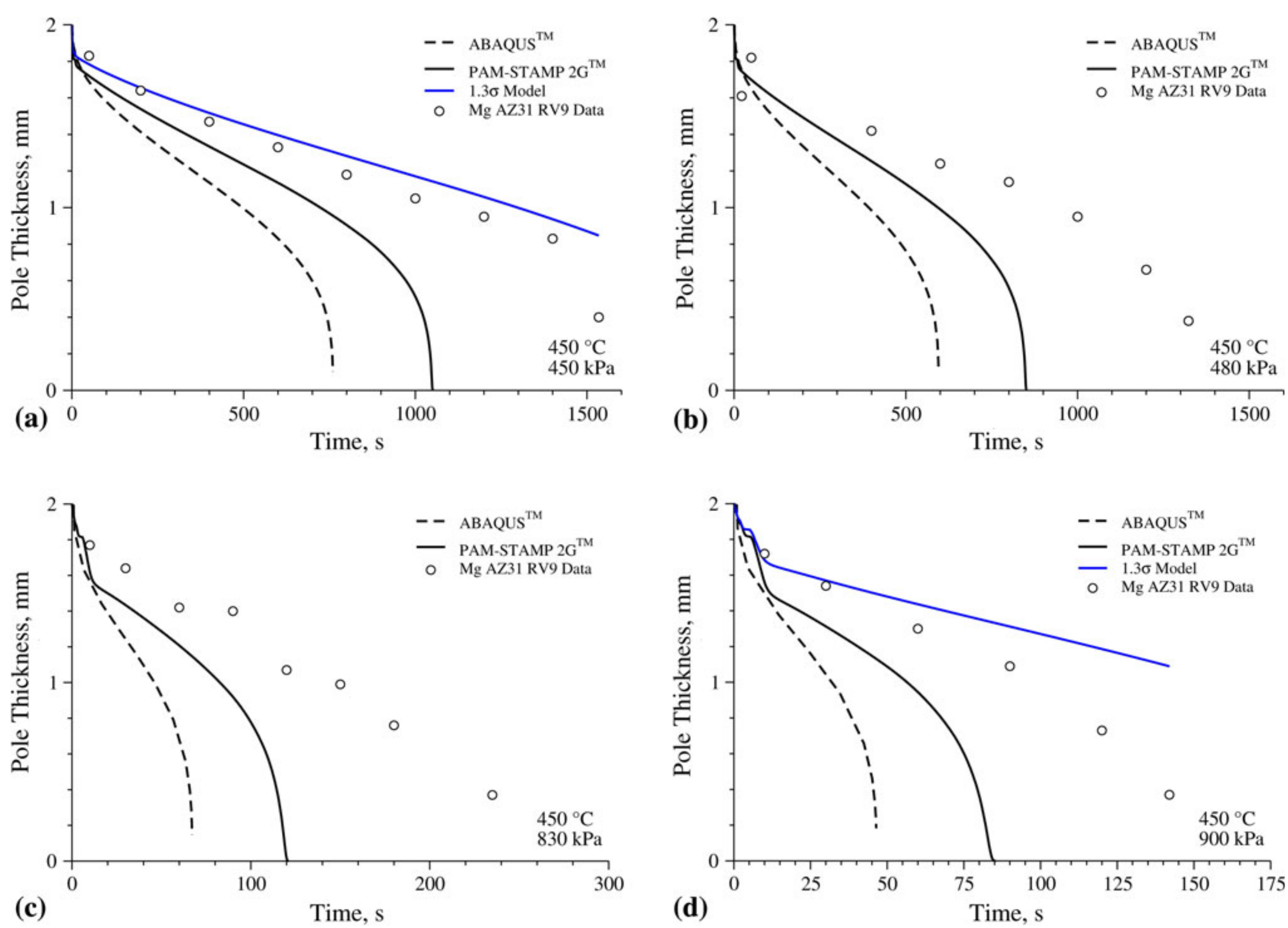

Fig. 5 Predictions for AZ31 dome pole thickness as a function of forming time are shown along with experimental bulge data at 450 °C, (a) 450 kPa (65 psi), (b) 480 kPa (70 psi), (c) 830 kPa (120 psi), and (d) 900 kPa (130 psi)

AZ31 sheet bulge forming, which use Eq 3 for material constitutive behavior, deviate significantly from experimental data. These deviations result largely from the failure of the material model to accurately predict AZ31 flow when biaxial tensile stresses predominate (i.e. primarily at the dome pole). Clearly, the observed deviations between simulation and experiment suggest that the AZ31 material behaves differently in biaxial tension than in uniaxial tension. Specifically, AZ31 flow under biaxial tension is in reality slower compared to that in uniaxial tension at the same effective (von Mises) stress at large Z values.

Results from the present study of AZ31 are thus markedly different from previous AA5083 studies. In Ref 18, it was shown that at small stresses and high temperature (i.e. low Z values where GBS creep dominates), AA5083 deformation is faster under balanced biaxial tension than under uniaxial tension. This difference between stress states in AA5083 disappeared at higher Z values, where solute-drag creep dominates deformation. At low Z values, GBS creep is thought to dominate deformation in AZ31. Yet for AZ31, the biaxial tensile stresses under bulge forming produce slower deformation than is predicted using the initial material model at low forming pressures (i.e. at low Z values). As pressure increases (i.e. as Z increases), AZ31 is expected to deform by a dislocation creep process. Unlike the AA5083 material, AZ31 continues to deform more slowly under the biaxial tension of bulge forming than is predicted using the initial material model. Moreover, the apparent deviation between actual forming rates and predicted forming rates using the material model from tensile data increases with increasing pressure.

Three potential sources of the differences between AZ31 material behavior under uniaxial tension and under biaxial tension can be identified. The first is the strong anisotropy of Mg alloy sheet materials. This is not indicated in the R-value measured from tensile tests, which agrees with the expected decrease in plastic anisotropy at elevated temperatures, but anisotropy along the 45° orientation is still a possibility. This hypothesis can be examined by conducting uniaxial tests with coupons cut along different orientations relative to the rolling direction of the Mg sheet. The second source is related to a fundamental effect of stress state on flow behavior. This second hypothesis has been suggested for fine-grained AA5083 materials (Ref 18), which appear to be affected by stress state, specifically the level of hydrostatic stress, when deformation is controlled by GBS creep. Unlike the AA5083 material, the AZ31 material appears to behave differently in uniaxial tension and in biaxial tension both in the GBS creep regime and in the dislocation creep regime. In fact, the effect of stress state appears to be greater in the dislocation creep regime than in the GBS creep regime for AZ31. Close examination of the tensile data of Fig. 1 reveals that some strain hardening occurs at the highest temperatures and slowest strain rates, i.e. low Z, where GBS creep is expected to control deformation. Such strain hardening is expected under GBS creep when grain growth occurs (Ref 20). However, strain hardening does not explain the differences between uniaxial and biaxial tension because these differences are also observed at the highest forming pressures, where GBS creep does not govern deformation and where strain hardening is not observed. A third source is dynamic recrystallization, a phenomenon which has been previously observed in AZ31 sheet materials during high-temperature deformation. Dynamic recrystallization has been observed to refine coarse grains in AZ31, but it could potentially lead to coarsening of a fine-grained material through discontinuous recrystallization into coarse grains. Neither of these effects is suggested by the tensile data, i.e. neither flow softening nor abrupt hardening is evident. Thus, further investigation is clearly warranted.

7. Conclusions

Two constitutive models for a fine-grained Mg AZ31 sheet material were developed and implemented into FE models of a gas-pressure bulge forming process at 450 °C. These constitutive models account for two independent creep mechanisms, viz., grain-boundary-sliding and slip creep, which are common to high-temperature forming of Al-Mg alloys. The first model is based solely on tensile SRC data. Relative to experimental results, the FE simulations using the first model predict faster forming at four (constant) pressures ranging from 450 kPa (65 psi) to 900 kPa (130 psi). In addition, faster thinning of the dome poles is predicted. In both cases, deviations between simulation and experiment are largest at the largest gas pressures. These results demonstrate that the initial material model based upon tensile SRC data does not accurately account for deformation of fine-grained Mg AZ31 sheet materials under a balanced biaxial tensile stress. However, a second material model introducing a shift to higher flow stresses, the 1.3 σ model, brings the simulation results into quite good agreement with bulge-forming measurements. Future effort must be therefore directed toward investigating the effects of microstructure evolution, in-plane anisotropy and the role of stress state on dome pole thinning. Such studies will help guide the development of Mg AZ31 material models that can be used to simulate forming of complicated part geometries, predict accurate strain distributions and assist with forming process optimization and prediction of part cycle times.

References

1. P.E. Krajewski and J.G. Schroth, Overview of Quick Plastic Forming, *Mater. Sci. Forum*, 2007, **551–552**, p 3–12
2. R. Verma and J.T. Carter, Quick Plastic Forming of a Decklid Inner Panel with Commercial AZ31 Magnesium Sheet, SAE Paper 2006-01-0525, 2006
3. PAM-STAMP 2G™. www.esigroup.com
4. ABAQUS™. www.simulia.com
5. J.T. Carter, P.E. Krajewski, and R. Verma, The Hot Blow Forming of AZ31 Mg Sheet: Formability Assessment and Application Development, *JOM*, 2008, **60**, p 77–81
6. E. Hsu, J.A. Szpunar, and R. Verma, Effect of Temperature and Strain Rate on Formability of AZ31 Magnesium Sheet Alloy, SAE Paper 2006-01-0258, 2006
7. A.-W. El-Morsy and K.-I. Manabe, Finite Element Analysis of Magnesium AZ31 Alloy Sheet in Warm Deep-Drawing Process Considering Heat Transfer Effect, *Mater. Lett.*, 2006, **60**, p 1866–1870
8. A.-W. El-Morsy, K.-I. Manabe, and H. Nishimura, Superplastic Forming of AZ31 Magnesium Alloy Sheet into a Rectangular Pan, *Mater. Trans.*, 2002, **43**, p 2443–2448
9. X. Wu and Y. Liu, Superplasticity of Coarse-Grained Magnesium Alloy, *Scr. Mater.*, 2002, **46**, p 269–274
10. K. Matsubara, Y. Miyahara, Z. Horita, and T.G. Langdon, Developing Superplasticity in a Magnesium Alloy Through a Combination of Extrusion and ECAP, *Acta Mater.*, 2003, **51**, p 3073–3084
11. H. Palaniswamy, G. Ngaile, and T. Altan, Finite Element Simulation of Magnesium Alloy Sheet Forming at Elevated Temperatures, *J. Mater. Process. Technol.*, 2004, **146**, p 52–60

12. C.F. Martin, J.J. Blandin, and L. Salvo, Variations in Microstructure and Texture During High Temperature Deformation of Al–Mg Alloy, *Mater. Sci. Eng. A*, 2001, **297**, p 212–222
13. K. Siegert and S. Jäger, Warm Forming of Magnesium Sheet Metal, SAE Paper No. 2004-01-1043, 2004
14. S. Kaya, Warm-Forming Aluminum and Magnesium. Part II: Determining Magnesium Sheet Properties at Elevated Temperatures, *Stamp. J.*, 2006, **18**, p 32–33
15. F.K. Abu-Farha and M.K. Khraisheh, Analysis of Superplastic Deformation of AZ31 Magnesium Alloy, *Adv. Eng. Mater. J.*, 2007, **9**, p 777–783
16. M.K. Khraisheh, F.K. Abu-Farha, and K.J. Weinmann, Investigation of Post-Superplastic Forming Properties of AZ31 Magnesium Alloy, *Ann. CIRP*, 2007, **56**, p 289–292
17. M.K. Khraisheh, F.K. Abu-Farha, M.A. Nazzal, and K.J. Weinmann, Combined Mechanics-Materials Based Optimization of Superplastic Forming of Magnesium AZ31 Alloy, *Ann. CIRP*, 2006, **55**, p 233–236
18. E. Taleff, L.G. Hector, Jr., J.R. Bradley, R. Verma, and P.E. Krajewski, The Effect of Stress State on High Temperature Deformation of Fine-Grained AA5083 Sheet, *Acta Mater.*, 2009, **57**, p 2812–2822
19. O.D. Sherby and P.M. Burke, Mechanical Behavior of Crystalline Solids at Elevated Temperature, *Prog. Mater. Sci.*, 1968, **13**, p 290–324
20. T.G. Nieh, J. Wadsworth, and O.D. Sherby, *Superplasticity in Metals and Ceramics*, Cambridge University Press, Cambridge, 1997, p 43–44
21. M.-A. Kulas, "Mechanical and Microstructural Characterization of Commercial AA5083 Aluminum Alloys," Ph.D. Thesis, Mechanical Engineering Department, The University of Texas at Austin, May 2004
22. W. Köster, Über eine sonderersheinung im temperaturgang von elastizitätsmodul und dämpfung der metalle kupfer, silber, aluminum und magnesium, *Zeitschrift für Metallkunde*, 1948, **39**, p 9–12